Numerical demonstration of a Dispersion Engineered Metallic Metasurface Assisted mm-wave Wireless Sensor

Sarath Sankar Vinnakota,[1,*] Runa Kumari,[1] Basudev Majumder,[2] and Qammar H. Abbasi[3]

[1]*Department of Electrical and Electronics Engineering. BITS-Pilani, Hyderabad Campus, Telangana, India 500078*
[2]*Department of Avionics, IIST Thiruvananthapuram, Kerala, India 695547*
[3]*James Watt School of Engineering, University of Glasgow, Glasgow, United Kingdom G12 8QQ*
[*]*sarath.vinnakota@gmail.com*

Abstract: In this paper, a metasurface-assisted multiport wireless power sensor is proposed and numerically verified for wireless power transfer (WPT) applications at mm-wave frequency band. A fully metallic 2D Luneburg lens constructed using glide symmetric unit cells, with a maximum gain of 18 dBi, acts as the radiating structure to receive the input RF power with a wide angular coverage range of $\pm 70^0$. A set of optimized class F rectifiers are integrated with this multiport lens using waveguide to microstrip transitions to obtain high power conversion efficiency over a wide angular space. These rectifying circuits are further connected for DC power combining, and a maximum power conversion efficiency of 72% is obtained at an input power level of 15.8 dBm.

1. Introduction

Wireless sensor nodes (WSN) are becoming increasingly common due to technological advances. They can be used in Internet of Things (IoT) applications for smart buildings to check environmental conditions, track human health, detect machine defects, and more [1]. However, higher operating powers are required for some of these applications. Wireless power transfer (WPT) is one of the approaches proposed to meet this power need.

With the advancements in technology, the base station for 5G has inadvertently become a reliable source of electricity and can function as an efficient wireless power grid. In contrast to the 3G and 4G frequency bands, the allowed effective isotropic radiated power (EIRP) in the mm-wave 5G band (>24 GHz) has been increased up to 75 dBm at a distance of 100 meters from the transmitter by the Federal Communications Commission (FCC) [2]. These high power densities open up the opportunity of powering the gadgets across long distances such as 5G base stations, as shown in Fig. 1. The consumption of batteries can be considerably decreased using this technique, and the life of sensor-based systems that require constant power can be extended. The article [3] elaborates on the options and the related critical challenges for the systems in the 5G frequency band and above. The works [2, 4, 5] attempted to explore the 5G wireless grid to study the performance of rectennas in this band.

A WPT receiver consists of the directive, minimal loss, wide-band receiving antennas with a wide field of view and the rectifier that aids in converting the received RF power into DC power with high radiation efficiency to drive a low-power wireless sensor node [6], [7]. Hybrid and passive beam-forming techniques in the form of Butler Matrix that are often used in phased array design to provide wide angular coverage and phase shift no longer remain a wise choice since at the mm-wave band the substrate becomes lossy. Moreover, the transmission lines start radiating [8, 9]. Conventional large aperture antennas seem to have satisfied the needs but their bandwidth and field of view are very narrow. Earlier the articles [2, 4] use lens-based approaches

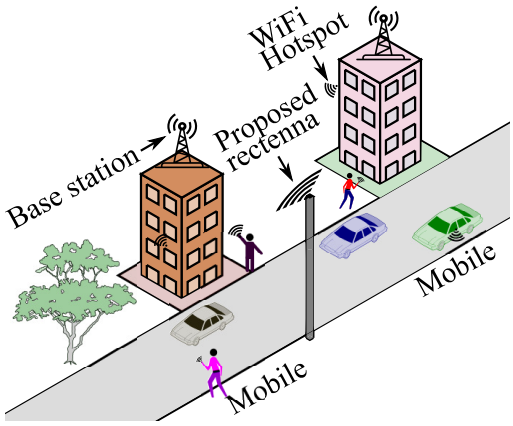

Fig. 1. Proposed system

but their angular coverage obtained is low and is not continuously tunable, respectively. This article looks for a best possible solution for a directive wide band and wide field of view switched beam antennas that can be useful for WPT applications. On the other hand, it is numerically and experimentally verified in [10] that increasing the number of antenna ports linearly increases the average output DC power at the load. Harvesting from a wide field of view (FOV) is always advantageous because the relative orientation of the source and the harvester is not known. In the recent past, the authors in [11] and [12] have designed 3D cylindrical patch arrays and Vivaldi antennas, respectively, to overcome this issue. However, their study is restricted to the lower frequency band. In [2] authors have used the Rotman lens integrated patch antennas to address this issue at the mm-wave band and achieved 110^0 scanning range. Moreover, Recently, metamaterial-based structures are being implemented to improve the gain of the antennas and for EM wave manipulation at microwave frequencies [13, 14]. The metasurface-inspired lens antennas being multi-port, unidirectional, and low profile can be an excellent candidate for WPT applications. The higher symmetries of the periodic structures such as twist, glide, or polar glide symmetry [15] have recently gained major popularity. These symmetries properly combined with transformation electromagnetic principle [16] can invent different types of electromagnetic devices such as lenses [17], with improved functionalities. A detailed study on the benefits of having glide symmetry to enhance the electromagnetic (EM) properties of the periodic structures such as dispersion, bandgap, anisotropy, and magnetic response is reported in [18]. It also describes various applications that use glide symmetric Luneburg lenses. A Luneburg lens is a spherically symmetric gradient-index lens whose refractive index (RI) η decreases radially from the center to the outer surface according to the equation [19].

$$\eta = \sqrt{\varepsilon_r} = \sqrt{2 - (r/R)^2} \tag{1}$$

Previous works such as [20] report the metamaterial-inspired microwave Luneburg Lens with varying refractive index. In addition, Gutman lenses using artificial dielectrics are also reported to improve the FOV [21]. There is a fundamental trade-off when simultaneously aiming to achieve a large FOV and large receiving aperture. The work [22] discusses the constraints usually observed when aiming for such a scenario. Using a multi-port antenna is one way to break the trade-off, which is the method used in this work. However, unlike [22], the proposed antenna aims for a wider FOV and that is achieved by multiple ports of the antenna receiving RF power simultaneously while operating independently of each other. By this method, irrespective of the position of the RF power source, as long as it is in the field of view of the antenna, the rectifier networks connected to the antenna convert the received RF power into DC power for further

usage by the sensor networks. In this way, the antenna is able to steer/switch the beam from a wider angular space and also can receive the power from a wider range and can act as a position insensitive wireless detector. Another vital design aspect for rectenna systems is the rectifier circuit that is realized using topologies like single series, voltage multipliers, etc., to improve the RF to DC power conversion efficiency (PCE), which is the primary equation used to evaluate the performance of the rectifying circuit for WPT applications, given by [5]

$$\eta_{PCE}(\%) = \frac{V_{out}^2}{R_L * P_{RF}} * 100 \tag{2}$$

where V_{out} is the output DC voltage, R_L is the load resistance and P_{RF} is the received RF power by the rectifier. Class F rectifier topology explored in [23, 24] employing RF Schottky diodes comes with improved PCE compared to the conventional topologies. Thus class F rectifier is selected here in this work to improve the efficiency of the overall rectenna.

The authors in [4] proposed rectifier integrated metallic Luneburg lens for WPT in 5G mm-wave band. The design has two major challenges. Firstly, a wide and continuous FOV is not covered and secondly, the PCE produced over a fixed RF power density is restricted to a relatively lower range. In [25] authors have proposed a dielectric-based metasurface lens with an inverse class F rectifier for wireless power transfer. However, the presence of dielectric is not suitable for high frequency applications as well as does not fit in the rugged and harsh environment. Moreover, the dielectrics at the high frequency prove to be lossy and systems made up of all metals are generally preferred. Thus, to bridge this gap, the requirement of a mm-wave metallic wireless power sensor operating at 5G frequency in a harsh environment having a wide coverage range along with a good PCE for a fixed available input RF power has inspired our study. To improve the coverage range, optimized waveguide to microstrip transitions that work in the operating band are introduced and to upgrade the PCE, a class F rectifier topology is designed and integrated with the optimized transitions. In class F rectifiers, at odd order harmonics, the load termination is open and at even harmonics, the load termination is short. The phenomenon is vice versa for inverse class F rectifiers where the load is open at even order harmonics and short at odd harmonics. The proposed multi-port directional metallic metasurface-based Luneburg lens is designed using the glide symmetric-based approach. The lens being fully metallic in nature and free from complex passive feed networks is less lossy at the mm-wave frequency band and also has a low cost. The currents obtained from the individual rectifiers are summed at a common optimized load.This combination offers a low-cost solution for making 5G suitable for the wireless power grid. Unlike [11] and [12] the proposed system operates over a widest possible angular range at mm-wave band frequencies to obtain highest PCE in mm wave band and also does not use any extra radiator integrated with the luneburg lens beam-former like [12] thereby making the footprint more robust and compact and suitable for harsh environment.

The lens structure, along with a detailed analysis of the unit cell, comparison between the glide symmetry and the non-glide version and their results are described in section II. Further, sections III and IV present the rectifier circuit and its integration to the lens to investigate the DC power combining.

2. Design of 2D Lens

2.1. Unit cell design and analysis

The proposed design of the lens consists of two metallic layers made up of several unit cells. Unlike [4], here, a comparative investigation in terms of its full Bloch mode analysis is done between the proposed unit cell with its non-glide version to investigate the bandwidth improvement and low dispersion at the higher frequencies. To have a deeper understanding of the wave propagation inside these metasurfaces, the detailed modal analysis and the isofrequency

contours have been studied. The top layer is obtained by shifting the bottom layer using the glide symmetry ($x \rightarrow x + p/2$, $y \rightarrow y + p/2$, $z \rightarrow -z$). In contrast, the top layer of the non-glide symmetry is obtained by mirroring the bottom layer ($z \rightarrow -z$). The top and bottom layers together form the unit cell, and there is a gap (g) of 0.3 mm between them. The periodicity of the unit cell is p, the length of the corrugations is s, and the height of the corrugations is indicated by h as shown in Fig. 2 for glide symmetric unit cell.

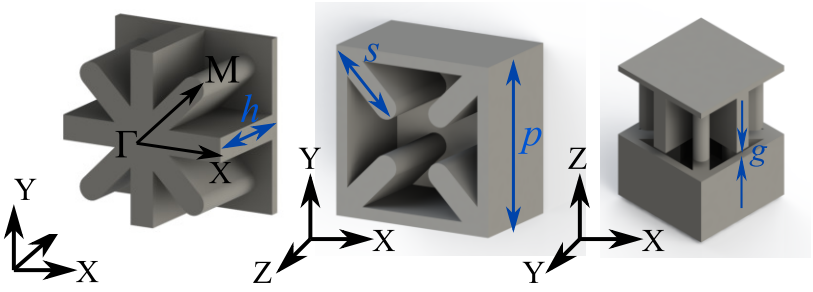

Fig. 2. Glide symmetric unit cell construction showing top, bottom and isometric views: h is height of the extrusion, s is the length of extrusion, p is the unit cell periodicity, g is the gap between unit cells

The dispersion diagrams for the first two modes for non-glide and glide symmetry are plotted in Fig. 3 for the highest refractive index (1.45) and lowers refractive index (1.06) values. The lowest two modal behaviors are obtained for the first irreducible Brillouin zones i.e., $\overline{\Gamma X}$ and $\overline{\Gamma M}$ as can be seen from Fig. 3(a).

The phase is normalized to unity. An important observation that can be made from these modal behaviors plotted in Fig. 3 (a) and (b) is that the glide symmetric unit cells do not produce any stop band zone. The two lowest order modes that appeared to be branching from the common point are actually a part of the same modal behavior. This fact has been further corroborated by the z component of the electric field distribution (E_Z) plotted in Fig. 4. The perfect correlation of the modal fields along the X directions in Fig. 4(a) and (b) confirm the same. But in the case of $\overline{\Gamma M}$ directions the modal field plots plotted in Fig. 4 (c) and (d) at the branching point of the two lowest order modes (at 40 GHz) show that there is in-fact zero correlation between them. These modal transitions can also be seen in the presence of the Dirac points in the photonic crystal [26]. The behavior of the modal fields for glide and non-glide is in perfect correspondence with the results computed with the help of the correlation theory [27, 28]. From the above explanations through the modal analysis, it can be concluded that the proposed glide symmetric unit cell allows the frequency to propagate till 40 GHz. In contrast, the non-glide counterpart limits its operation due to the presence of a strong band gap between 25.9 GHz to 43.5 GHz. The frequency response of the glide and non-glide unit cells given in Fig. 5, characterized using an indirect characterization method for the X direction propagating wave, provides insightful evidence of the same. Fig. 5(a) shows a strong dip in propagation at the same frequency band between 25.9 GHz and 43.5 GHz. On the contrary, the frequency response of the glide counter-part shows complete propagation till 40 GHz. To gain a deep understanding of the relevant consequences of directional properties of the proposed unit cell through different directions, the isofrequency curves for both glide and non-glide are reported in Fig. 6. It shows that using glide symmetry, the spatial dispersion occurring due to mode 1 is minimized, making the isofrequency curves more circular in nature over a wide band of frequency. Thus, the wave propagation through it becomes more isotropic. For non-glide symmetry, the curves tend to become more elliptic as a consequence of having distinct phase velocities along different directions. The study of the modal behaviors of the electromagnetic wave through the glide symmetric unit cell is significant in the

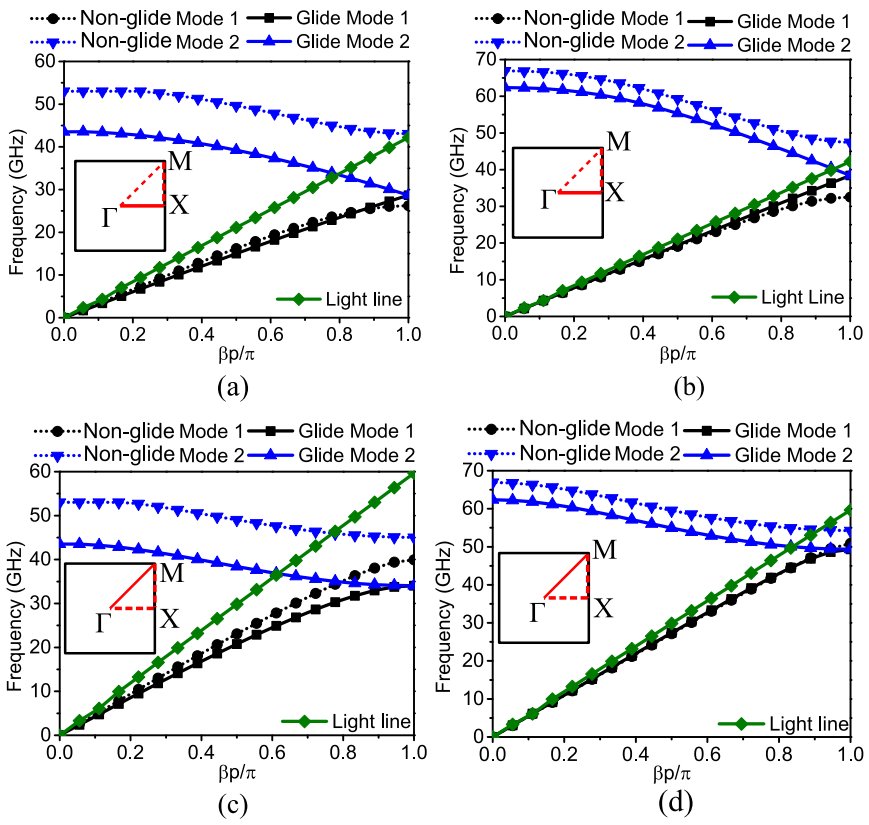

Fig. 3. Dispersion diagram for modes 1 and 2 with corresponding irreducible brillouin zones for (a) highest RI (s_1 = 1.85 mm, h_1 = 2 mm, $\overline{\Gamma X}$) (b) lowest RI (s_5 = 0.7 mm, h_3 = 0.5 mm, $\overline{\Gamma X}$) (c) highest RI (s_1 = 1.85 mm, h_1 = 2 mm, $\overline{\Gamma M}$) (d) lowest RI (s_5 = 0.7 mm, h_3 = 0.5 mm, $\overline{\Gamma M}$)

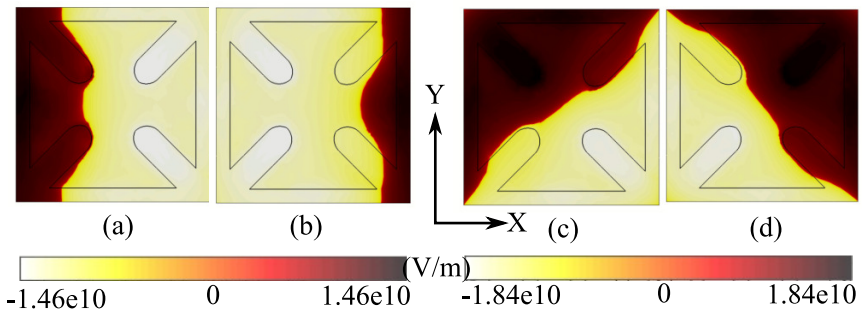

Fig. 4. Electric fields (E_z) for highest RI (a) $\overline{\Gamma X}$) Mode 1 (b) $\overline{\Gamma X}$ Mode 2 (c) $\overline{\Gamma M}$ Mode 1 (d) $\overline{\Gamma M}$ Mode 2

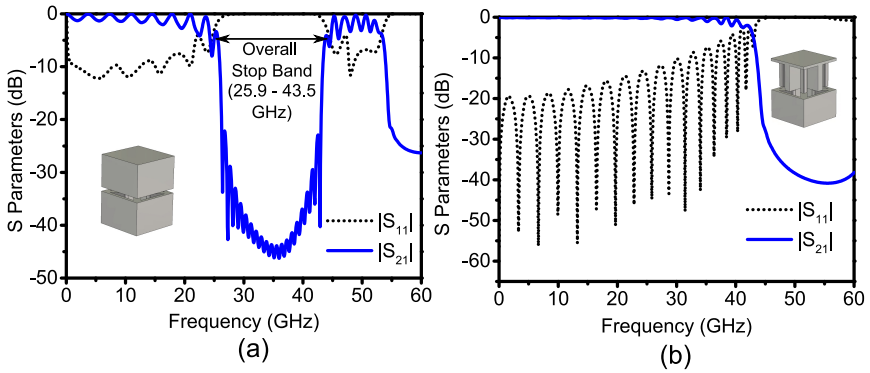

Fig. 5. For Mode 1 (a) Non-glide (b) Glide

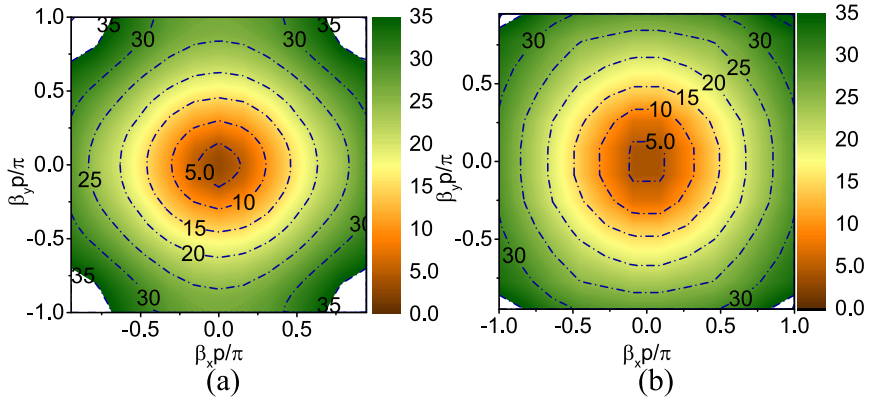

Fig. 6. Isofrequency curves comparing the (a) Non-glide unit cell and (b) Glide symmetric unit cell for highest refractive index (1.45) at 26.5 GHz

context of constructing a wide band isotropic and less dispersive engineered surface responsible for focusing the radiation.

The modal differentiation between glide and non-glide has been verified further with the help of the multi-modal Bloch analysis [29] in Fig 7 using the Floquet ports through the first Brillouin zone $\overline{\Gamma X}$. The unit cells have been simulated in the frequency domain solver, and 3 higher order modes have been considered in the port modes to construct the scattering responses accurately. The lowest order mode has been used to extract its propagation constant. Fig. 7(a) and (b) report that the results computed using the eigenmode analysis and the multimodal Bloch analysis match completely. The advantage of using the Bloch analysis is that it can calculate the attenuation constant per period (α/p). The non-glide unit cells in Fig. 7(a) show a higher attenuation constant over the band-gap zone. On the contrary, the glide version in Fig. 7(b) indicates ideally no attenuation. The real part of the extracted refractive index profile of the lens is presented in Fig. 8 for both the glide and non-glide versions using the Effective Medium Theory approach. It can be seen from these figures that the glide version shows strong dispersion with respect to frequency (bandwidth limited). On the contrary, the glide counterpart shows a more uniform variation of the extracted refractive index over a wide frequency bandwidth. The period of the unit cells being very small as compared to its operating wavelength, the surface can ideally behave like a homogenized surface of the extracted material parameters. We withdrew from studying the detailed characterization of its material parameters since these have already

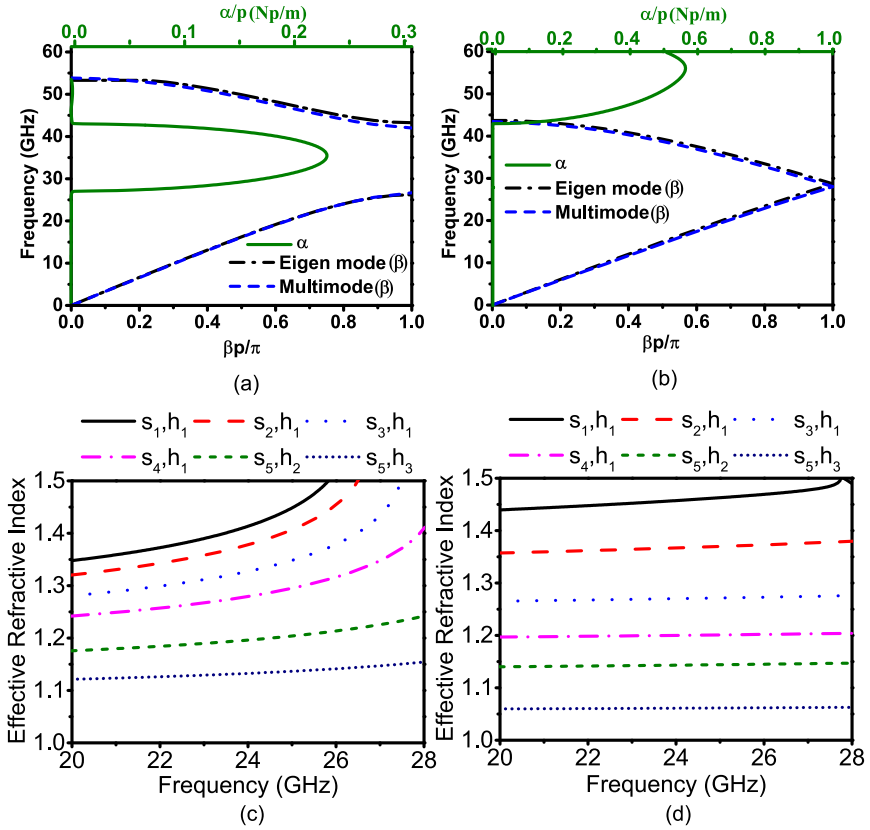

Fig. 7. Comparison of attenuation, eigen mode and bloch mode characterizations of (a) Non-glide (b) Glide ;Effective refractive index plotted with varying frequency for (c) Non-glide unit cell (d) Glide symmetric unit cell. Dimensions (in mm): s_1 = 1.85, s_2 = 1.6, s_3 = 1.35, s_4 = 1.1, s_5 = 0.7, h_1 = 2, h_2 = 1 and h_3 = 0.5

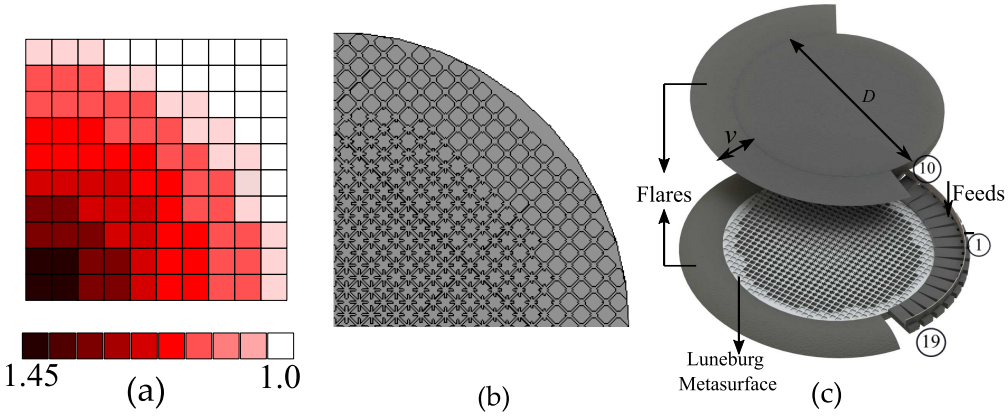

Fig. 8. (a) Refractive index variation with the unit cell design and construction of lens for one quadrant (b) Construction of one quadrant of lens (c) Exploded view of the lens: D = 118 mm, v = 24 mm

been studied in [4]. Modulating the glide not only gives extra bandwidth suitable for a wider range of operation but also provides a very low dispersion over the wider bandwidth which is very important to attain the isotropicity in the phase velocity profile of propagating wave inside the lens medium. The broken symmetry did allow that to happen by minimizing the stop band between its bottom two propagating modes as can be seen in Fig, 7(b). As a result, the lowest propagating mode attains a linear profile. On the contrary, for the non-glide case, even if the geometrical tuning may give a wider range of bandwidth in the lowest propagating modes, it doesn't minimize the band gap between the two bottom propagating modes and the bottom mode remains frequency dispersive resulting in an elliptical isofrequency contour and varying material parameters. The physical insight for the same has been discussed in Fig. 7(c) and (d) and also in [29].

2.2. Design and analysis of the all metal Luneburg lens

The 2D Luneburg refractive index profile is created initially in order to construct the lens. The desired refractive index and the related dimensions in terms of radius are then obtained by developing an equivalent dielectric lens using the extracted material parameters. The lens is then built from the unit cell in the following step by discretizing the obtained RI profile for a single quadrant. Due to the discretization operation, the cells produced are periodically positioned along the X and Y axes in accordance with the predicted refractive index profiles and the corresponding dimensions. The final design is then formed by extending the lens from the quadrant employing the mirror and circular symmetries. The detailed steps of the design can be found in [4]. The work [30] discusses the discretization of the two-dimensional Luneburg lens based on the correctional effective medium theory. The entire lens is reconstructed by using this profile to cover all four quadrants, and a flare structure designed similar to the one in [4] is added to match the aperture impedance to the free space as shown in Fig. 8(a). The diameter of the lens D is set to 118 mm, so that the antenna achieves a specific beamwidth of 6.3^0, to satisfy the ranges suitable for WPT applications. The design of the feeding network is presented in Fig. 9. Unlike [4], the present structure is fed by a waveguide to microstrip transition [31] which uses a standard WR28 waveguide. In this proposed work, the feed waveguide part of the structure is modified and optimized by adding E-plane step transitions to work in the required frequency range. The microstrip transition consists of an E-field probe tuned to cancel the imaginary part of the impedance and allows for maximum coupling of the electric field between the waveguide (TE_{10} mode) and the microstrip line (quasi TEM mode). The probe is placed approximately at a distance of $\lambda/4$, indicated by b in Fig. 9, from the back-short end of the waveguide to effectively couple the E-field and obtain a better impedance matching. The entire structure is designed on RT Duroid 5880 substrate with a thickness of 0.254 mm. The optimized dimensions of the waveguide and the transition structure are shown in the inset of Fig. 9. The reflection coefficient response of the waveguide and the transition combined from this graph confirms that the transition is suitable for use at the desired frequency range.

The advantage of using this waveguide to microstrip transition is to allow the structure to cover a wider and continuous scanning range compared to [4], where the latter used direct microstrip feed that limited the coverage between -36^0 and $+36^0$ only with discrete scanning angles.The feeding structure is then used as the input to the radiating lens structure, and the structure is excited using a discrete port. The remaining feeds are symmetrically placed on either side of the central feeding structure to expand the lens coverage. The entire EM simulation is carried out in commercial software CST MWS 2021. The S-parameter response is reported in Fig. 10, and the impedance bandwidth can be observed between 24.5 and 27.5 GHz which falls in the 5G communication band [32] as seen from Fig. 10(a).The cross-talk between the ports is shown in Fig. 10(b) and is observed to be less than -20 dB. This plot proves that very less power leaks into the undesired ports, and the majority of the accepted input power is fed efficiently to the lens

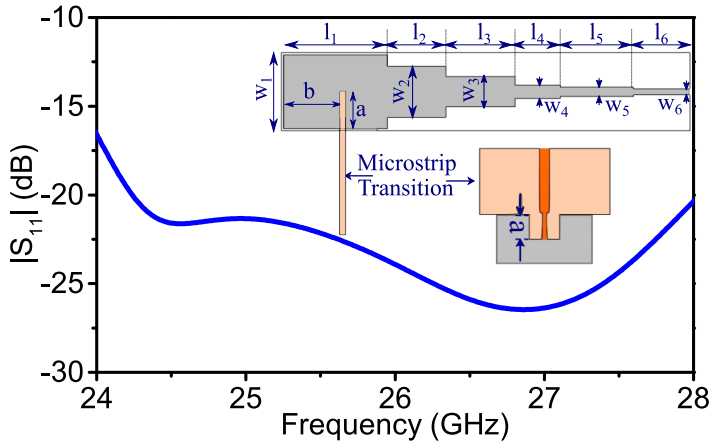

Fig. 9. Waveguide to Microstrip transition design and S_{11} plot: l_1 = 5, l_2 = 2.8, l_3 = 3.33, l_4 = 2.18, l_5 = 3.51, l_6 = 2.7, w_1 = 3.556, w_2 = 2.45, w_3 = 1.46, w_4 = 0.636, w_5 = 0.44, w_6 = 0.3; In inset: a = 1.8, b = 2.717 (all dimensions in mm)

medium.

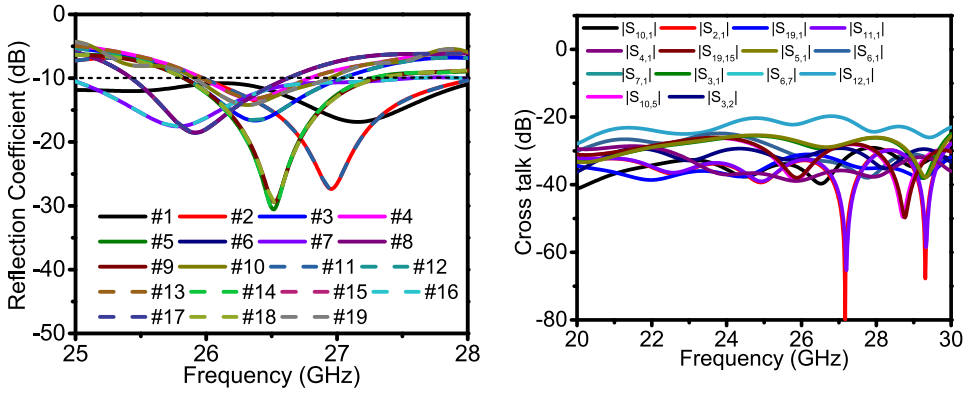

(a) (b)

Fig. 10. (a) Reflection coefficients for each of the antenna ports (b) Cross talk between the antenna ports

The normalized radiation patterns of the structure for all the ports at 26.5 GHz are shown in Fig. 11, and the plot shows that the structure provides wide coverage of 140^0 (from -70^0 to $+70^0$), showing an improvement of 32^0 more than [2] and 68^0 more than [4]. The other plane also shows a fan beam pattern covering a beamwidth of 6.3^0 as illustrated in Fig. 15(a). The maximum gain of 18 dBi is obtained at port 1 with all other ports giving the gain of more than 16.5 dBi at 26.5 GHz frequency. The radiation efficiency is defined as the ratio of gain to directivity and is directly calculated from the EM simulation tool CST MWS. It is noted to be more than 68% for all the ports with a maximum of 87% at port 1. This calculation also includes the metallic losses.

3. Design and analysis of single unit of rectifying element

The class-F rectifier topology provides higher efficiency than conventional topologies and is thus selected to make the rectifier circuit. It uses a shunt Schottky diode as the non-linear device for

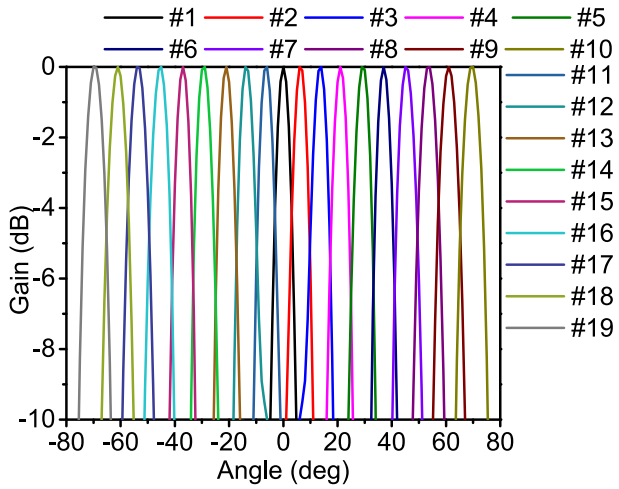

Fig. 11. Normalized radiation pattern of the antenna, (θ=90^0)

the frequency of operation at 26.5 GHz as shown in Fig. 12(a). The same substrate used for the waveguide to microstrip transition is used for the rectifier design. The shunt diode is followed by a harmonic termination network consisting of two open stubs with an electrical length of $\lambda/8$ and $\lambda/12$ along with a series stub with an electrical length of $\lambda/4$ at 26.5 GHz. The stubs are

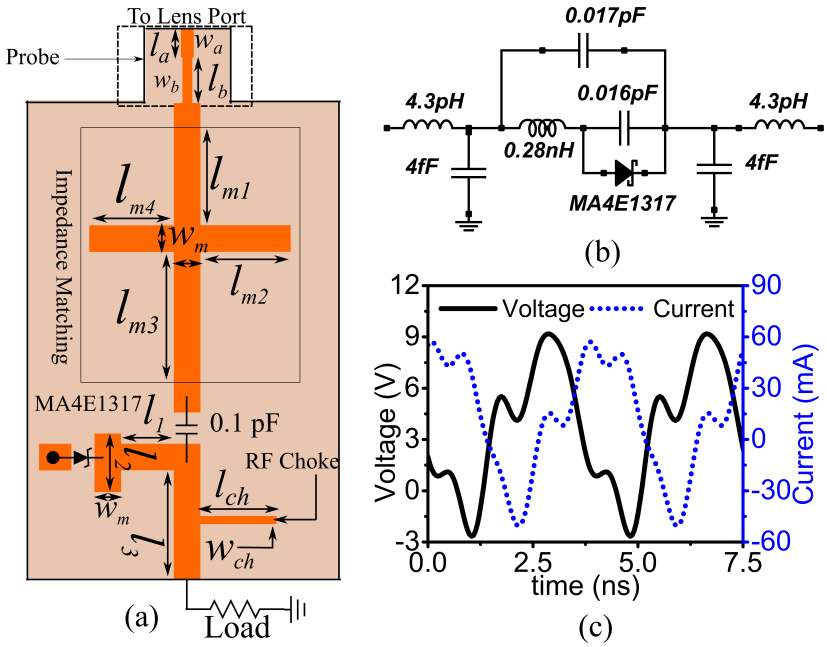

Fig. 12. (a) Rectifier circuit at 26.5 GHz: l_{m1} = 1.49, l_{m2} = 4.92, l_{m3} = 15.6, l_{m4} = 4.92, l_1 = 2.75, l_2 = 1.72, l_3 = 5.78, l_{ch} = 2.134, w_{ch} = 0.228, w_m = 0.78, w_a = 0.35 w_b = 0.28, l_a = 0.8, l_b = 1.25 (b) Schottky diode model with parasitics (c) Voltage and Current variation across the diode

designed using commercial software ADS and optimized such that the overall structure acts as a low pass filter, and its transmission coefficient is close to 0 dB at 26.5 GHz. The Schottky

diode used for the design is MA4E1317 which is previously used for the same band in [5, 33]. The diode model with parasitics is shown in Fig. 12(b) is taken from the Schottky diode model validated in [34] for a similar frequency band. [5, 33] is selected and is connected at the input of the designed filter. For the final rectifier design, the voltage and current waves across the diode are shown in Fig. 12(c).

Different parametric studies are carried out to analyze the optimum input power and the load to determine the PCE. The input power varies from 5 to 25 dBm and the PCE is calculated for various load values as seen from Fig. 13(a). It is noted that the maximum value is 75.4% for 530Ω at 15.8 dBm input power. Further, another parametric study shown in Fig. 13(b) conducted with load swept from 0 to 1200 Ω for different input powers also shows maximum efficiency of 75.4% at 15.8 dBm. Taking these values of load and input power, the reflection coefficient is

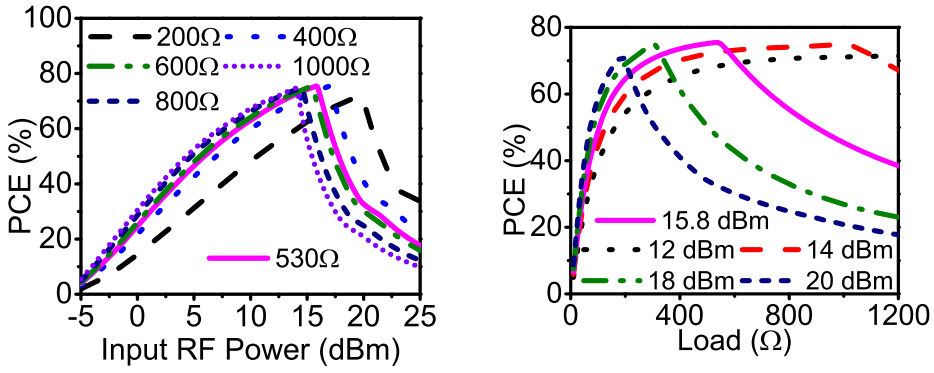

Fig. 13. Variation of (a) PCE with RF power at various load values (b) PCE with load at various input power levels

plotted for frequency variation as shown in Fig. 14(a). It is observed that the designed matching network performs well for the input powers varying from 12 dBm up to 18 dBm. Finally, the PCE is also plotted for various input powers with frequency swept from 26 to 27 GHz shown in Fig. 14(b). A consistent PCE above 50% is observed for the input powers with a maximum value of 75.4% at 26.5 GHz for the same input power of 15.8 dBm. Taking all these parameters into account, it is finally concluded that the PCE is maximum for 15.8 dBm input power and 530 Ω load and reaches 75.4%.

4. Rectifier-Lens Integration and DC power combining

The Z-parameters of the overall lens structure obtained from CST MWS contain the impedance information for all the ports throughout the desired frequency range. The ports of the rectifier are interlinked to the Z-parameter data obtained in the previous step, thereby replicating the antenna impedance matrix Z_A, followed by the class F rectifying circuits as illustrated in Fig. 15(a). The impedance matching networks are implemented with symmetric open stubs and the lengths are calculated by optimizing the stub length such that the reflection coefficient at the desired frequency is minimized for each port. The outputs from the class F rectifiers are subsequently connected to combine the power and deliver it to a common load, as shown in Fig. 15(b). The load to the combined circuit can be obtained by dividing the optimized load by the number of rectifier stages and is calculated as 27.8 Ω. The PCE and the total output DC voltage obtained with the circuit, are shown in Fig. 15(c). It can be observed from Fig. 15(c) that the total output DC voltage varies non-linearly with the input RF power, and it reaches a value of 3.8 V at an

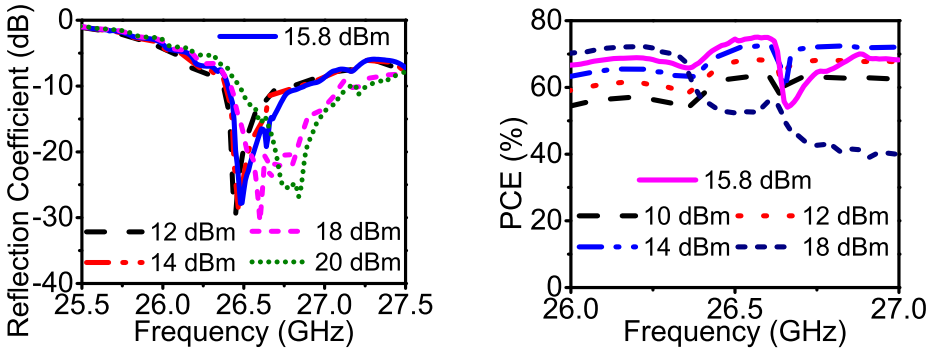

(a) (b)

Fig. 14. At various input power levels (a) reflection coefficient with frequency (b) PCE with frequency

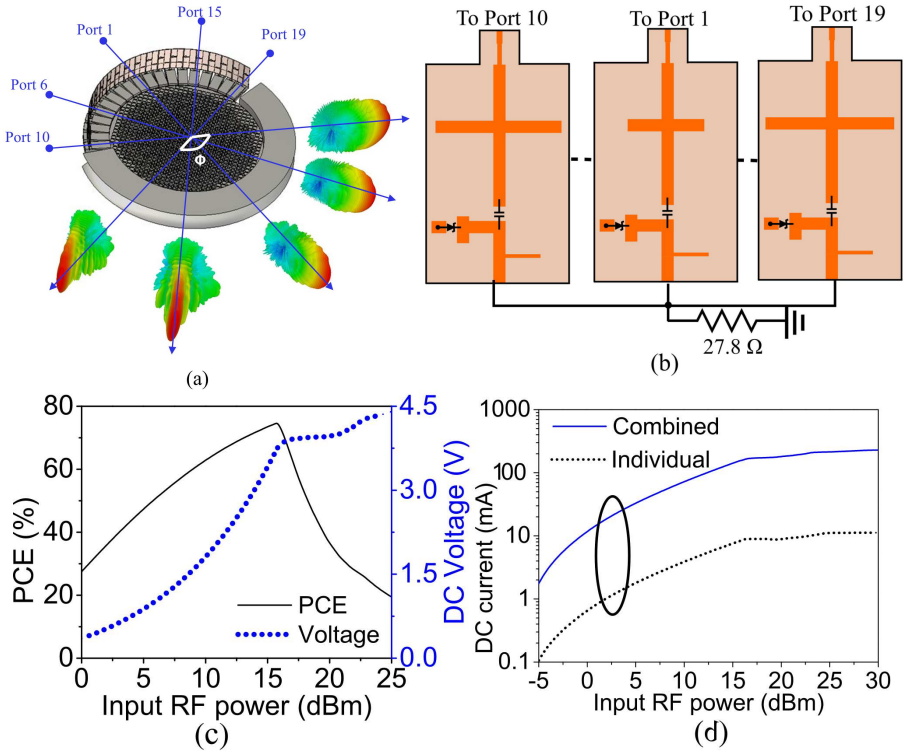

Fig. 15. (a) Integrated lens and rectenna (ϕ=140^0, for clarity only a few radiation patterns are shown)(b) DC power combining network (c) Output DC power and PCE with varying input power at 26.5 GHz (d) DC current improvement after combining

input power of 15.8 dBm as depicted in Fig. 15(c).

At the input power of 15.8 dBm, the maximum PCE is found to be 72 %, as shown in Fig.15(c) and the output DC power starts going into saturation. Similarly, the output DC across the load increases by more than a 10-fold logarithmic factor due to DC combining, as seen in Fig. 15(d). It can be noted that the proposed system combines all the received power from each port to deliver the maximum efficiency at the optimized load. If the power comes from a particular direction, the optimized load value of the single unit rectifier should be readjusted by dividing the number of active ports only to get the highest possible efficiency without changing the rest of the circuit. Also, the proposed system has the flexibility to drive the single optimized load from the active ports if required. The performance of the proposed sensor system is compared with the state-of-the-art in Table 1. The works quantify the error between simulation and measurement by percentage.

It can be seen from Table I that, the majority of the works [35–39] are concentrated in the lower frequency range and do not have the capability of the beam steering/switching. So, they are unsuitable for harvesting power from a wide angular space. Though the works reported in the references [5, 24, 31, 40–42] have attempted energy harvesting at high-frequency band targeting the mm-wave band, they also don't possess the beam steering or switching capability. Very recently in [2] authors have proposed the importance of a directive beam steering antenna for harvesting mm wave power at 28 GHz from a wide angular range to sum up the delivered dc power from each port. But since at a very high frequency implementing passive systems on microstrip platforms with conventional transmission lines prove to be lossy. So it has still been a challenge to design a directive beam steering less lossy antenna for harvesting power from a wide angular range. In [25], authors have proposed a dielectric-based medium for the same, but that is not suitable for carrying high power and also is not robust and thus, is not recommended to be used in an EM-sensitive environment. The possibility of dielectric breakdown of the high-cost material is an added disadvantage too. The losses present in the material at high frequency are prone to produce a higher level of signal attenuation. So, in this paper, an all-metal monolithic Luneburg lens is proposed for the same which can incur less loss and harvest from a wider range of angles. Besides the metal being low cost in nature and easily accessible can be fabricated using low-cost 3D printing or CNC micro-machining technique for large-scale operation. Also, the presence of the harmonically controlled class F rectifier topology to produce good PCE by collecting the dc output power makes it unique and novel.

5. Conclusion

A DC power combining rectifier circuit network is designed and integrated with a Luneburg lens for the WPT application at 26.5 GHz. The radiating lens has 19 ports giving a maximum gain of 18 dBi and spans a coverage area from -70^0 to +70^0. The overall metasurface-assisted rectenna system gives a maximum PCE of 72% at 15.8 dBm power and can be used to drive a wireless sensor node. This proposed passive robust system can create a new window for long-range 5G power RFID devices for wearable and ubiquitous IoT applications.

Acknowledgement

The necessary support for the graduate studies is provided by the University Grants Commission, India (No. 3746, NET-July 2018). This work is carried out within the framework of DST Inspire Faculty Award (IFA17-ENG197). The authors thank Prof. Oscar Quevedo-Teruel from KTH Royal Institute, Sweden for technical discussions. The authors acknowledge the computation time by High Performance Computation facility "Sharanga" by BITS-Pilani, Hyderabad Campus for carrying out the required simulations.

Table 1. Comparison with published works employing Schottky diodes (* - simulated, # - absolute power)

Ref	Freq (GHz)	Antenna Design	Diode (Topology)	Eff.(%) at Power	Gain (dBi)	Beam Steering	Remarks
[35]	0.9	Coplanar Dipole	Skyworks (Class F)	48.6 ($8\mu W/cm^2$)	2.3	No	Flexible, Omni-directional, low cost, eliminated matching network
[36]	2.45	Patch antenna	SMS 7630 (Class F)	72^* (0 dBm)$^\#$	NA	No	Flexible, Broad beamwidth
[37]	2.45	Monopole antenna	HSMS 2810 (Class F)	82 (34 dBm)$^\#$	6.5	No	Flexible, High PCE
[38]	2.45	Differential antenna	BAT-64 (Class F)	73 (22 mW/cm^2)	NA	No	Circular polarization and dual port differential feed rectifier
[39]	5.8	Aperture coupled antenna array	HSMS 286C (Class F)	72 (15 dBm)$^\#$	15	NA	High Gain, High PCE
[40]	19.5	Aperture coupled antenna array	MA4E1317 (NA)	77.9 (8.5 mW/cm^2)	19.5	No	Dual polarization, High PCE for various tilt angles
[24]	24	NA	MA4E1317 (Class F)	65.9 (NA) (NA)	NA	No	High efficiency
[5]	24	SIW backed antenna	MA4E1317 (Self bias)	45 (10 mW/cm^2)	10.3	No	2×2 array with Circular polarization
[41]	24	Flexible antenna	MA4E1319 (Voltage doubler)	12 (10 dBm)$^\#$	8	No	High gain, Broadband, Wearable rectenna
[2]	28	Rotman Lens	MA4E2038 (Single Series)	NA (12 dBm/cm^2)	17	Yes	High gain, Long range, Flexible
[31]	35	NA	MA4E1317 (Single Series)	68.5 (39.3 mW/cm^2)	NA	No	High PCE, Low loss, Shielded microstrip line with waveguide feed
[42]	35.7	4×4 patch antenna array	MA4E1317 (Single Series)	67 (7 mW)$^\#$	19	No	High gain, Good PCE
Prop.*	**26.5**	**Metallic Luneburg Lens**	**MA4E1317 (Class F)**	**72 (15.8 dBm)**$^\#$	**18**	**Yes**	**Low cost, Wide coverage angle, Low loss, Waveguide feed**

Disclosures

The authors declare no conflicts of interest.

Data Availability

Data underlying the results presented in this paper are not publicly available at this time but may be obtained from the corresponding author upon reasonable request. within the article.

References

1. R. J. Vullers, R. v. Schaijk, H. J. Visser, J. Penders, and C. V. Hoof, "Energy Harvesting for Autonomous Wireless Sensor Networks," IEEE Solid-State Circuits Mag. **2**(2), 29–38 (2010).
2. A. Eid, J. G. D. Hester, and M. M. Tentzeris, "5G as a wireless power grid," Sci. Rep. **11**(1), 636 (2021).
3. U. Gustavsson, P. Frenger, C. Fager, T. Eriksson, H. Zirath, F. Dielacher, C. Studer, A. Pärssinen, R. Correia, J. N. Matos, D. Belo, and N. B. Carvalho, "Implementation Challenges and Opportunities in Beyond-5G and 6G Communication," IEEE J. Microwaves **1**(1), 86–100 (2021).
4. S. S. Vinnakota, R. Kumari, H. Meena, and B. Majumder, "Rectifier Integrated Multibeam Luneburg Lens Employing Artificial Dielectric as a Wireless Power Transfer Medium at Mm Wave Band," IEEE Photon. J. **13**(3), 1–14 (2021).
5. S. Ladan, A. B. Guntupalli, and K. Wu, "A High-Efficiency 24 GHz Rectenna Development Towards Millimeter-Wave Energy Harvesting and Wireless Power Transmission," IEEE Trans. Circuits Syst. I, Reg. Papers **61**(12), 3358–3366 (2014).
6. F. Congedo, G. Monti, L. Tarricone, and V. Bella, "A 2.45-GHz Vivaldi Rectenna for the Remote Activation of an End Device Radio Node," IEEE Sens. J. **13**(9), 3454–3461 (2013).
7. Y.-S. Chen and J.-W. You, "A Scalable and Multidirectional Rectenna System for RF Energy Harvesting," IEEE Trans. Compon. Packag. Manuf. Technol. **8**(12), 2060–2072 (2018).
8. D.-J. Lee, S.-J. Lee, I.-J. Hwang, W.-S. Lee, and J.-W. Yu, "Hybrid Power Combining Rectenna Array for Wide Incident Angle Coverage in RF Energy Transfer," IEEE Transactions on Microwave Theory and Techniques **65**(9), 3409–3418 (2017).
9. J. J. Kuek, K. T. Chandrasekaran, M. F. Karim, Nasimuddin, and A. Alphones, "A compact Butler matrix for wireless power transfer to aid electromagnetic energy harvesting for sensors," in *2017 IEEE Asia Pacific Microwave Conference (APMC)*, pp. 334–336 (2017).
10. S. Shen, Y. Zhang, C.-Y. Chiu, and R. Murch, "Directional Multiport Ambient RF Energy Harvesting System for the Internet of Things," IEEE Internet Things J. pp. 1–1 (2020).
11. E. Vandelle, D. H. N. Bui, T.-P. Vuong, G. Ardila, K. Wu, and S. Hemour, "Harvesting Ambient RF Energy Efficiently With Optimal Angular Coverage," IEEE Transactions on Antennas and Propagation **67**(3), 1862–1873 (2019).
12. C. Song, P. Lu, and S. Shen, "Highly Efficient Omnidirectional Integrated Multiband Wireless Energy Harvesters for Compact Sensor Nodes of Internet-of-Things," IEEE Transactions on Industrial Electronics **68**(9), 8128–8140 (2021).
13. S. D. Assimonis, S. Chandravanshi, O. Yurduseven, D. Zelenchuk, O. Malyuskin, M. A. B. Abbasi, V. Fusco, and S. L. Cotton, "Implementation of Resonant Electric Based Metamaterials for Electromagnetic Wave Manipulation at Microwave Frequencies," Sensors **21**(24), 8452 (2021).
14. X. Wan, T. Y. Chen, X. Q. Chen, L. Zhang, and T. J. Cui, "Beam Forming of Leaky Waves at Fixed Frequency Using Binary Programmable Metasurface," IEEE Transactions on Antennas and Propagation **66**(9), 4942–4947 (2018).
15. O. Quevedo-Teruel, G. Valerio, Z. Sipus, and E. Rajo-Iglesias, "Periodic Structures With Higher Symmetries: Their Applications in Electromagnetic Devices," IEEE Microw. Mag. **21**(11), 36–49 (2020).
16. O. Quevedo-Teruel, W. Tang, R. C. Mitchell-Thomas, A. Dyke, H. Dyke, L. Zhang, S. Haq, and Y. Hao, "Transformation optics for antennas: why limit the bandwidth with metamaterials?" Sci Rep **3**(1), 1903 (2013).
17. Q. Liao, N. J. G. Fonseca, and O. Quevedo-Teruel, "Compact Multibeam Fully Metallic Geodesic Luneburg Lens Antenna Based on Non-Euclidean Transformation Optics," IEEE Transactions on Antennas and Propagation **66**(12), 7383–7388 (2018).
18. O. Quevedo-Teruel, Q. Chen, F. Mesa, N. J. G. Fonesca, and G. Valerio, "On the Benefits of Glide Symmetries for Microwave Devices," IEEE J. Microw. **1**(1), 457–469 (2021).
19. R. Luneburg, *Mathematical Theory of Optics* (University of California Press, 2021).
20. Y. L. Loo, Y. Yang, N. Wang, Y. G. Ma, and C. K. Ong, "Broadband microwave Luneburg lens made of gradient index metamaterials," J. Opt. Soc. Am. A **29**(4), 426–430 (2012).
21. P. Bantavis, C. G. Gonzalez, R. Sauleau, G. Goussetis, S. Tubau, and H. Legay, "Broadband graded index Gutman lens with a wide field of view utilizing artificial dielectrics: a design methodology," Opt. Express **28**(10), 14,648–14,661 (2020).

22. R. Fatemi, P. P. Khial, A. Khachaturian and A. Hajimiri, "Breaking FOV-Aperture Trade-Off With Multi-Mode Nano-Photonic Antennas," IEEE Journal of Selected Topics in Quantum Electronics, **27**(1),1-14 (2021).
23. J. Guo, H. Zhang, and X. Zhu, "Theoretical Analysis of RF-DC Conversion Efficiency for Class-F Rectifiers," IEEE Trans. Microw. Theory Techn. **62**(4), 977–985 (2014).
24. K. Hatano, N. Shinohara, T. Mitani, K. Nishikawa, T. Seki, and K. Hiraga, "Development of class-F load rectennas," in *2011 IEEE MTT-S Int. Microw. Workshop Series on Innovative Wireless Power Transmission: Tech., Syst., and Appl.*, pp. 251–254 (2011).
25. B. Majumder, S. S. Vinnakota, S. Upadhyay, and K. Kandasamy, "Dielectric Metasurface Inspired Directional Multi-Port Luneburg Lens as a Medium for 5G Wireless Power Transfer—A Design Methodology," IEEE Photonics Journal **14**(3), 1–10 (2022).
26. W.-Y. He and C. T. Chan, "The Emergence of Dirac points in Photonic Crystals with Mirror Symmetry," Scientific Reports **5**(1), 8186 (2015).
27. A. Coves, S. Marini, B. Gimeno, and V. Boria, "Full-Wave Analysis of Periodic Dielectric Frequency-Selective Surfaces Under Plane Wave Excitation," IEEE Transactions on Antennas and Propagation **60**(6), 2760–2769 (2012).
28. M. Bozzi, S. Germani, L. Minelli, L. Perregrini, and P. de Maagt, "Efficient calculation of the dispersion diagram of planar electromagnetic band-gap structures by the MoM/BI-RME method," IEEE Transactions on Antennas and Propagation **53**(1), 29–35 (2005).
29. Q. Chen, F. Mesa, X. Yin, and O. Quevedo-Teruel, "Accurate Characterization and Design Guidelines of Glide-Symmetric Holey EBG," IEEE Transactions on Microwave Theory and Techniques **68**(12), 4984–4994 (2020).
30. Z. Sun, C. Liu, R. Xu, H. Gong, X. Xuan, R. Liu, M. Du, and H. Cao, "Discretization of two-dimensional Luneburg lens based on the correctional effective medium theory," Opt. Express **29**, 33434-33444 (2021)
31. Q. Chen, Z. Liu, Y. Cui, H. Cai, and X. Chen, "A Metallic Waveguide-Integrated 35-GHz Rectenna With High Conversion Efficiency," IEEE Microw. Wireless Compon. Lett. **30**(8), 821–824 (2020).
32. M. J. Marcus, "ITU WRC-19 Spectrum Policy Results," IEEE Wirel. Commun. **26**(6), 4–5 (2019).
33. A. Riaz, S. Zakir, M. M. Farooq, M. Awais, and W. T. Khan, "A Triband Rectifier Toward Millimeter-Wave Frequencies for Energy Harvesting and Wireless Power-Transfer Applications," IEEE Microw. Wireless Compon. Lett. **31**(2), 192–195 (2021).
34. Q. Chen, X. Chen, H. Cai, and F. Chen, "A Waveguide-Fed 35-GHz Rectifier With High Conversion Efficiency," IEEE Microw. Wireless Comp. Lett. **30**(3), 296–299 (2020).
35. S. Korhummel, D. G. Kuester, and Z. Popović, "A harmonically-terminated two-gram low-power rectenna on a flexible substrate," in *2013 IEEE Wireless Power Transfer (WPT)*, pp. 119–122 (2013).
36. J. Zhang and Y. Wang, "A Flexible Wearable Rectenna for Wireless Energy Harvesting," in *2019 8th Asia-Pacific Conference on Antennas and Propagation (APCAP)*, pp. 128–129 (2019). ISSN: 2642-9179.
37. G. Wang, J. Zhang, Y. Wang, and Q. Guo, "A Graphene Film-based Rectenna for Wireless Power Transmission," in *2019 IEEE Asia-Pacific Microwave Conference (APMC)*, pp. 1566–1568 (2019).
38. S. Chandravanshi, D. Zelenchuk, and N. Buchanan, "A Rectenna Design Based on Circularly Polarized Differential Antenna and Class-F Rectifier," in *2021 15th European Conference on Antennas and Propagation (EuCAP)*, pp. 1–5 (2021).
39. C. Yu, F. Tan, and C. Liu, "A C-band microwave rectenna using aperture-coupled antenna array and novel Class-F rectifier with cavity," Journal of Electromagnetic Waves and Applications **29**(8), 977–991 (2015).
40. L. Li, J. Du, and X.-X. Yang, "Dual Polarized Rectenna and Array at X-band with High-Efficiency," in *2019 International Conference on Microwave and Millimeter Wave Technology (ICMMT)*, pp. 1–3 (2019).
41. M. Wagih, G. S. Hilton, A. S. Weddell, and S. Beeby, "Broadband Millimeter-Wave Textile-Based Flexible Rectenna for Wearable Energy Harvesting," IEEE Trans. Microw. Theory Techn. **68**(11), 4960–4972 (2020).
42. A. Mavaddat, S. H. M. Armaki, and A. R. Erfanian, "Millimeter-Wave Energy Harvesting Using 4×4 Microstrip Patch Antenna Array," IEEE Antennas Wirel. Propag. Lett. **14**, 515–518 (2015).